

NANOMATERIALS UNDER MECHANICAL ACTIONS

R.A. Andrievski

Institute of Problems of Chemical Physics, Russian Academy of Sciences,
Semenov Prospect, 1, Chernogolovka, Moscow Region, 142432, Russia

Received: November 23, 2015

Abstract. Nanomaterials (NMs) usually exist in non-equilibrium state. Thus, the NMs stability in extreme environments is a very crucial problem. Here, this overview is devoted to mainly current researches of the NMs behavior under various mechanical actions. The effect information connected with the cyclic loading, equal-channel angular pressing (ECAP), high-pressure torsion (HPT), and other mechanical actions (including combined those) on the structure, phase transitions, and properties of NMs, is generalized and considered in detail. In addition, some theoretical approaches and modeling are described. The importance of additional studies is underlined.

1. INTRODUCTION

The stability issue is particularly relevant for NMs because they usually are metastable in nature. Many features, such as numerous interfaces (in the form of grain boundaries and triple junctions), as well as a possible presence of some non-equilibrium phases, segregations, residual stresses, and pores, determine the deviation from the equilibrium state and the availability of the Gibbs free energy excess in nanostructures. But on the other hand, it is non-equilibrium that leads to a significant increase of the physical and mechanical properties and allows production of NMs with unique characteristics. Currently, the operation conditions of many modern devices and units are progressively changing towards increasing the thermal, mechanical, radiation, corrosive, and other combined impacts of the environment, not to mention the time of service. Such a tendency requires a special attention to the NMs behavior and stability under listed extremes, as well as the search for new NMs withstanding the extreme environments. Thus, the NMs stability in ex-

treme environments presents a very crucial problem.

It should be noted in general that the behavior of substances and conventional coarse-grained (CG) materials under extreme conditions is also currently attracting increasingly greater interest (e.g., [1–5]). Despite the fact that materials and substances are frequently studied in different ranges of temperatures, pressures, and other parameters, however, there are always certain intervals of overlap, and therefore undoubtedly, these results are complementary and contribute to better understanding. The author and other scientists have considered some features of the NMs behavior at high temperatures, as well as under irradiation and corrosion actions (e.g., [6–20]). Mechanical actions are very widely used in the NMs manufacture methods, such as consolidation of nanopowders, multivariate severe plastic deformation (SPD) of metallic bulk materials, etc. (e.g., [21–23]). However, the information about the actual NMs behavior under the influence of different loads seems to be not sufficient and extensive. In this regard, the

Corresponding author: R.A. Andrievski, e-mail: ara@icp.ac.ru

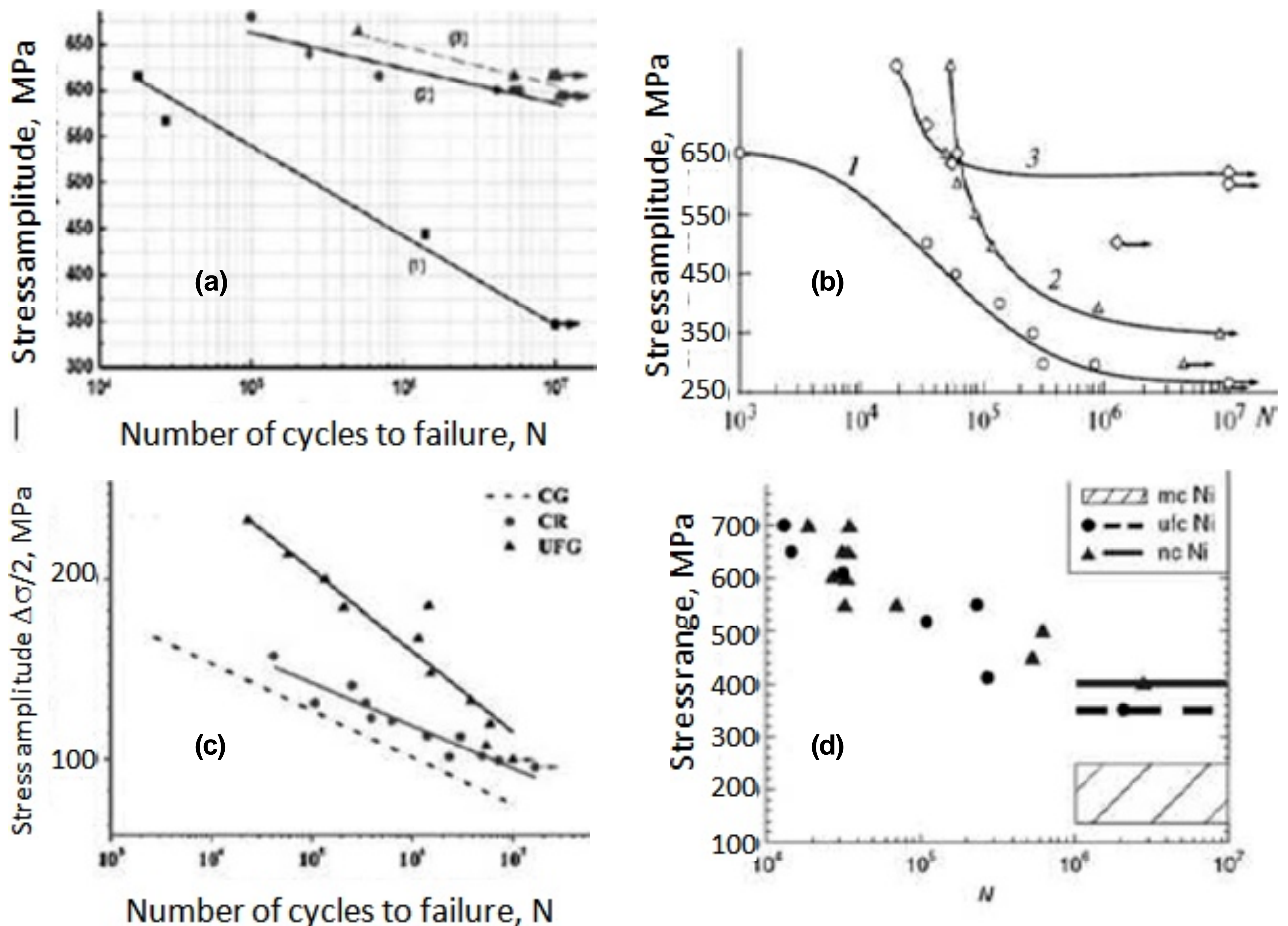


Fig. 1. Dependences of the stress amplitude on number of cycles to failure for Ti (**a**, adapted from [26]), steel (**b**, adapted from [27]), Cu (**c**, adapted from [28]), and Ni (**d**, adapted from [29]).

a: CG Ti (curve 1, grain size $L \sim 30 \mu\text{m}$); UFG Ti after ECAP + thermal mechanical treatment (TMT) (curve 2, $L \sim 200 \text{ nm}$); UFG Ti after ECAP + TMT + annealing at $350 \text{ }^\circ\text{C}$ (curve 3, $L \sim 200 \text{ nm}$).

b: CG 321 stainless steel in initial hot-forged state (curve 1, $L = 20\text{--}30 \mu\text{m}$); CG after ECAP (curve 2, $L = 100\text{--}250 \text{ nm}$); CG after ECAP + annealing at $550 \text{ }^\circ\text{C}$ (curve 3, $L = 10\text{--}15 \mu\text{m}$).

c: CG Cu (curve - - -, $L \sim 150 \mu\text{m}$); cold-rolled (CR) Cu (curve ●); UFG Cu (curve ▲, $L = \text{mix} (500 \text{ nm} + 2 \mu\text{m})$).

d: mc Ni ($L = 5\text{--}15 \mu\text{m}$), ufc Ni ($L \sim 300 \text{ nm}$), nc Ni ($L = 20\text{--}40 \text{ nm}$).

proposed overview is devoted to a more detailed discussion of this issue.

2. EXPERIMENTAL STUDIES

2.1. Fatigue results

The possibility of to substantially increase the material strength by reducing the grain size has long attracted stirred interest in the analysis of fatigue characteristics of NMs (e.g., [22–25]). Let us consider the effect of ECAP on the fatigue properties by the example of comparative studies of titanium, 321 stainless steel, copper, and nickel samples [26–29]. The fatigue responses for ultrafine-grained (UFG) samples subjected to ECAP are presented in Fig. 1, allowing comparison them with the results with CG those.

It is evident from Fig. 1 that the advantages of Ti, stainless steel, Cu, and Ni UFG or nc samples remain valid for ordinary fatigue tests with $10^4\text{--}10^7$ cycles and the refinement by ECAP seems to be very useful. However, it is also obvious that the location of $S\text{--}N$ curves (stress–number of cycles to failure) for the studied objects are not the same: as N grows the difference in the $S\text{--}N$ curves for stainless steel and copper is reduced, this difference seems to be near constant for nickel and even increases for titanium case. The explanation of this difference for different metals/alloys is a challenging problem, due to the abundance of many factors, such as temperature of deformation and its character, texture and surface roughness, as well as the presence of twins and low-/high-angle grain boundaries, the role of impurities and alloying elements,

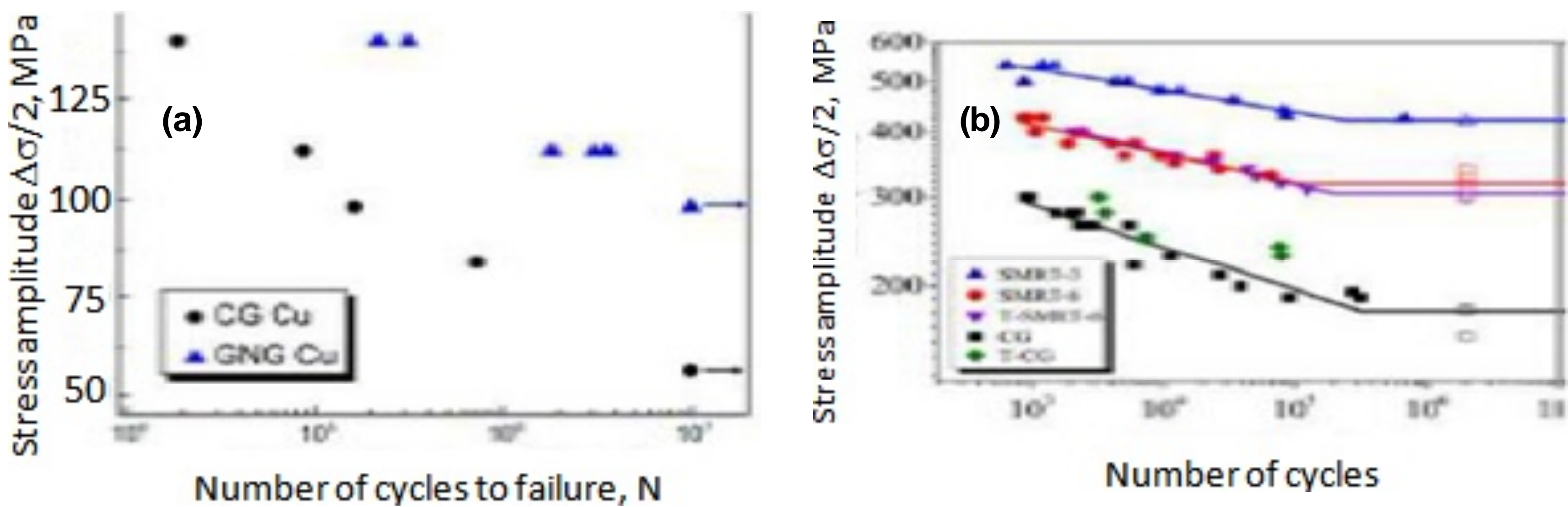


Fig. 2. S–N curves of different samples of Cu (a) processed by SMGT (● CG is initial coarse-grained sample ($L=0.5\text{--}5\ \mu\text{m}$); ▲ GNG is gradient nanograined one ($L=55\text{--}105\ \text{nm}$ in the top 15 mm thick layer and $L\sim 300\ \text{nm}$ in the depth of 75 μm)) and AISI 316L stainless steel (b) processed by SMRT (■ CG is initial coarse-grained sample ($L\sim 100\ \mu\text{m}$); ▲● are SMRT-3 and SMRT-6 samples with diameter 3 μm and 6 μm ($L<100\ \text{nm}$ in the top 40 μm thick layer and $L\sim 150\ \text{nm}$ in the depth of 170 μm); ▼◆ are SMRT-6 and CG samples after an uniaxial tensile strain of 3%, respectively. Adapted from [33,34].

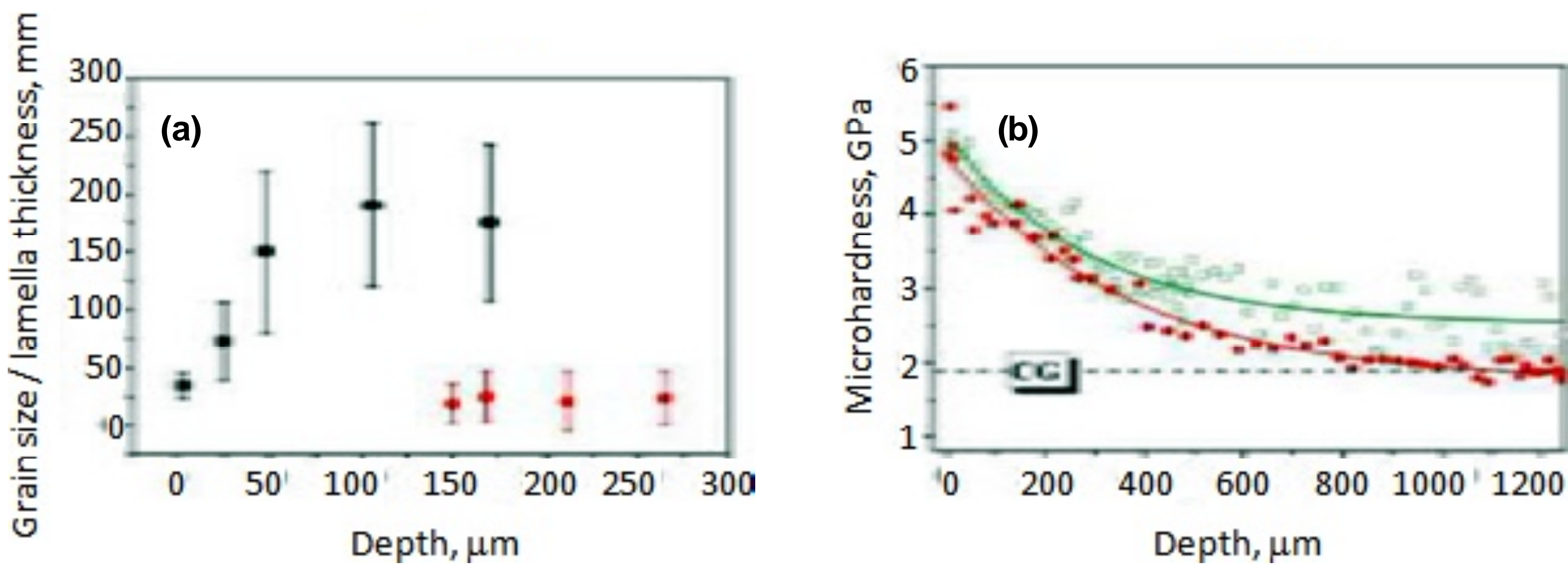


Fig. 3. (a) Grain size (■)/lamella thickness (●) and (b) the microhardness value of 316L stainless steel as function of distance from treated surface of the as-SMRT sample (●) and the SMRT one after fatigue at $\Delta\sigma/2 = 325\ \text{MPa}$ (□), adapted from [34].

the accumulation and propagation of cracks, the grain growth under cyclic loads, etc. [24,25,30]. The decisive influence on the fatigue strength has features of nucleation and propagation of microcracks, depending on the stress state, the presence of defects, grain characteristics, etc. The study of fatigue strength of thin films and nanowires showed that the number of cycles to failure increases with decreasing the Cu film thickness. It is interesting that the exceptional high strength of Cu–Si nanowires is at least saved or even improved during cyclic loadings, and this effect needs further clarification [31,32].

Compared to ECAP, the structure refinement was more effective for improving fatigue characteristics in the case of the use of other SPD techniques, such as surface mechanical grinding/attrition treatment (SMGT/SMAT). Fig. 2 shows the fatigue response of copper and AISI 316L austenitic stainless steel with a gradient nanograined surface layer (adapted from [33, 34]).

It is clearly seen from Fig. 2 that the surface deformation processing significantly improves fatigue properties in a practical manner uniformly in the low- and in the high-cycling fatigue regimes. In the case of conventional UFG copper processed by ECAP, the fatigue strength improvement was found to decrease markedly in the high-cycle fatigue range (see Fig. 1c, [28]). The most detailed study of the SMRT effect on the fatigue properties improvement has been performed as applied to gradient nanostructured surface layer of AISI 316L stainless steel [34]. The following main features can be pointed.

- 1) The sample diameter decrease was found to be more effective in the fatigue strength enhancement than preliminary deformation (Fig. 2b).
- 2) Detailed microstructure characterization of the surface layers using transmission electron microscopy (TEM), X-ray diffraction (XRD) and selected area electron diffraction permitted the revelation of variation of grain size and lamella thickness of twins

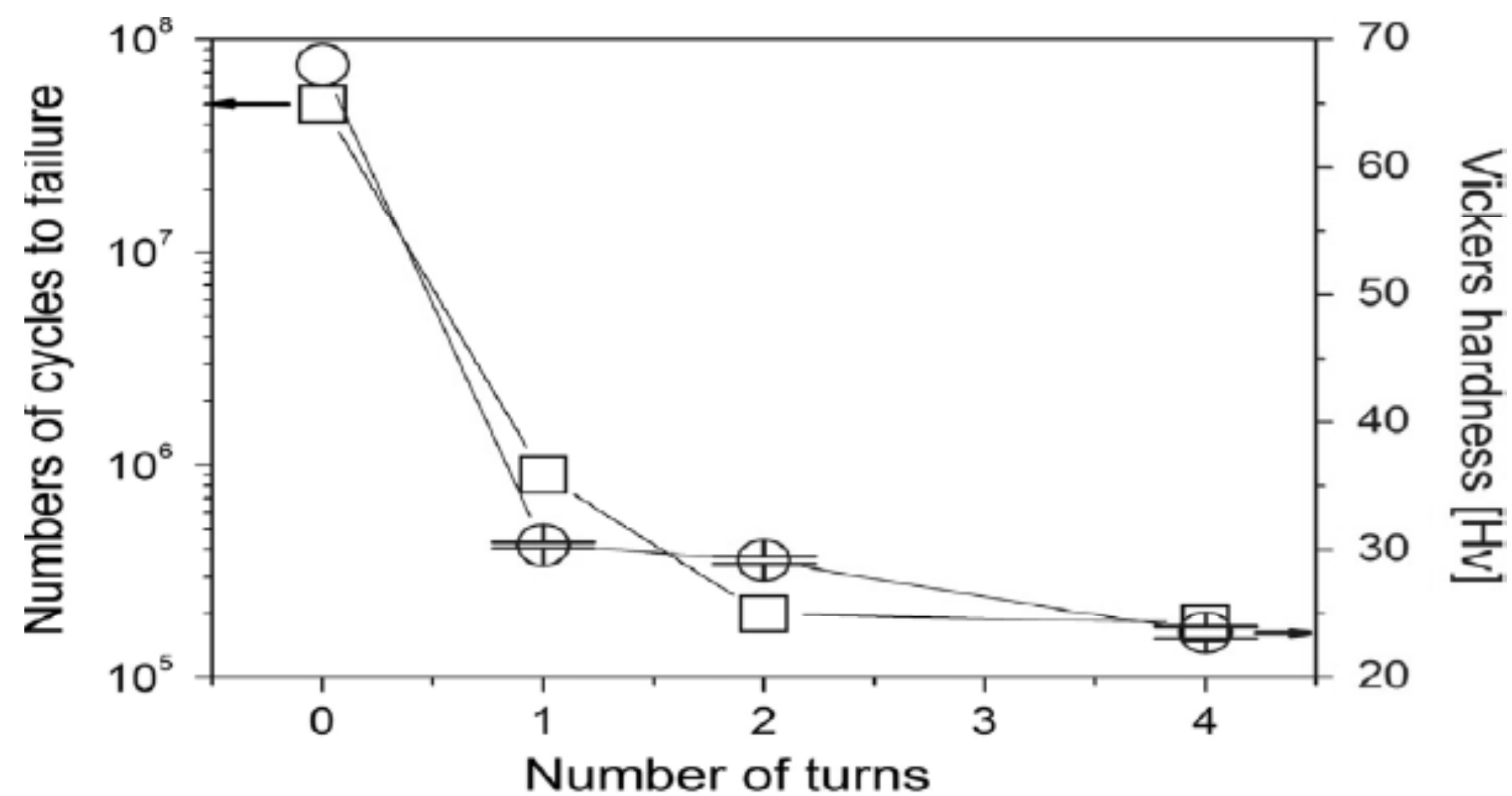


Fig. 4. The effect of the numbers of turns during HPT on fatigue life and Vickers hardness for Zn–22 wt.% Al alloy, adapted from [37].

values of mar-tensite phase forming from the prior austenite one. Fig. 3 shows variations of grain size/twin lamellar thickness and microhardness with depth in the SMRT sample (adapted from [34]).

As can be seen from Fig. 3, nanosized martensite grains ($L < 100$ nm) are formed in the top 40 μm surface layer and then the martensite grains increase with depth in the top 100 μm up to 170 nm. In the subsurface layer with a depth from 150 to 270 μm , the twin lamellar thickness of dominant austenite phase is about 25 nm. The length of total deformation zones in metals processed by SMRT/SMGT was about 20–60% of the rod initial radius. The detailed analysis of results [33,34] has shown that the gradient nanostructured surface layers not only contribute to the high fatigue strength, but also suppress crack nucleation.

Special attention is drawn to the NMs behavior under high-cycle fatigue tests, which can increase the formation of cracks on the grain boundaries (e.g., [35]). On the one hand, fatigue tests (in the range $N=10^8$ – $2 \cdot 10^{10}$ cycles) of UFG Cu after ECAP (the grain size of 300 nm) showed that the fatigue strength is twice that for conventional CG copper [36]. However, on the other hand, it was found that the increase in the number of turns through HPT (i.e., increasing the level of deformation and decreasing grain size) leads to lower numbers of cycles to failure and Vickers hardness (H_V) (Fig. 4, adapted from [37]).

The grain size L in the eutectoid alloy Zn–22% Al changed as follows: in the initial state it was 1400 nm; after 1 turn HPT $L = 400$ nm; after 2 turns $L = 370$ nm; after 4 turns $L = 350$ nm [37]. The noteworthy decrease in hardness with decreasing grain size is typical for superplastic alloys (e.g., [38]). It is interesting to clarify, if the picture of reduction in the fatigue strength with decreasing grain size, found for superplastic alloy Zn–22%Al, is typical for other

metals and alloys. In general, it should also be noted that the regularities in the NMs behavior in high-cycle fatigue require further investigation.

2.2. Phase transitions

It is well known that under high pressures the lattice may become unstable, which brings to the so-called deformation phase transitions and the emergence of structures with different symmetry. As regards to NMs, one should keep in mind the size dependence of phase stability and the emergence of new phase nuclei. For example, the grain size, below which martensite transformation during cooling of the alloy $\text{Ti}_{50}\text{Ni}_{25}\text{Cu}_{25}$ is not observed, is 15–25 nm, which is smaller than the size of a critical nucleus martensite phase, i.e., when $L < 15$ –25 nm for the alloy martensitic transformation stalls due to the inability of the embryos occurrence [39].

Alivisatos et al. [40] have investigated the size dependence of the pressure-induced γ to α structural phase transition in Fe_2O_3 nanocrystals in detail. The transition pressure was found to increase with decreasing grain size: annealed bulk samples transformed at 24 ± 2 GPa, 7 nm crystals transformed at 27 ± 2 GPa, 5 nm ones at 34 ± 3 GPa, and 3 nm ones at 37 ± 2 GPa. The authors [40] mention that the transition pressure increase was also revealed in other objects, such as PbS, ZrO_2 , Si, TiO_2 , etc., and the effect can be connected with both kinetic and thermodynamic reasons as well. In particular, the observed increase in nanocrystals can be attributed to both the surface energy contribution and of the nucleation points features for phase transitions.

To study of phase transitions and composition changes under mechanical effects, HPT is frequently used. As an example, Fig. 5 shows the dependence of the volume of the ω -phase for the $\alpha \rightarrow \omega$ Ti

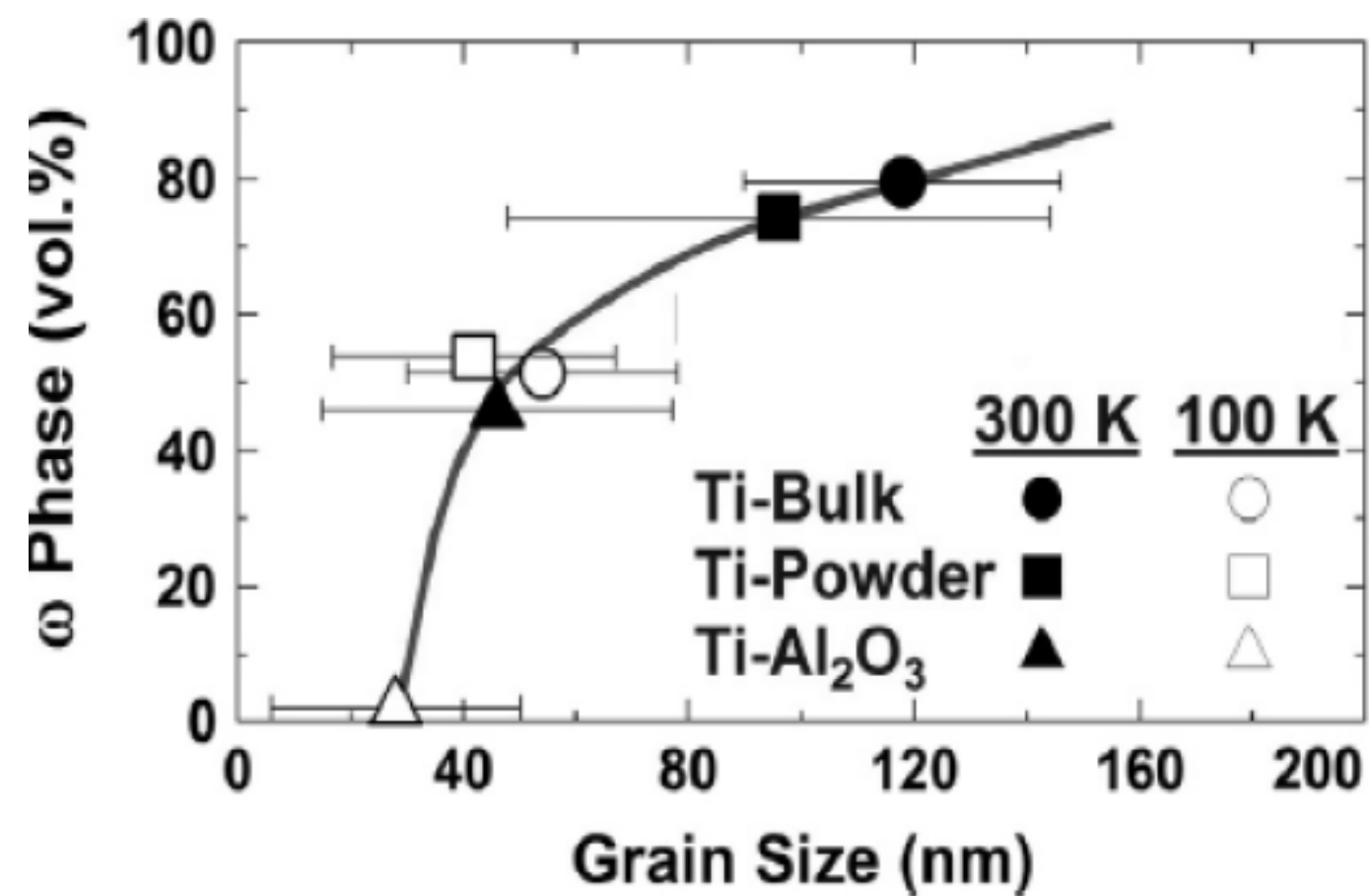


Fig. 5. The ω -phase fraction plotted vs. the average grain size for three Ti samples processed by HPT at room and cryogenic temperatures (adapted from [41]).

transformation on the grain size of different source samples at room and cryogenic temperatures ($P = 6$ GPa, number of turns $n = 10$) [41]. From Fig. 5 clearly follows that the formation of the ω -phase is significantly reduced with decreasing initial grain size and HPT temperature. For $L < 30$ nm and $T = 100$ K, the $\alpha \rightarrow \omega$ transformation is almost completely suppressed, which may be related to the impossibility of the ω -phase nucleation (as in the case described above for the $\text{Ti}_{50}\text{Ni}_{25}\text{Cu}_{25}$ alloy [39]).

The HPT effect on the change in the composition and properties of Fe–C and Al–Zn alloys, as well as ZnO due to the grain size variation has been investigated in Refs. [42–44]. It was shown that the solubility of manganese and cobalt in ZnO under HPT significantly with decreasing L [42]. The vanish of unstable Fe_5C_2 carbide and residual austenite in nanocrystalline Fe–1.7 wt.%C alloys was observed after HPT [43]. In addition, HPT favors in the presence of ~ 2 nm zinc layer on the Al grain boundaries in Al–30 wt.%Zn UFG alloy ($L \sim 400$ nm) [44]. Some examples of deformation-induced amorphization are presented and considered in review [45], where it is noticed that an accumulative roll bonding (ARB) of the multi-layer Cu–Zr composites is accompanied with amorphization, which can be connected with both a high dislocation density and mutual solubility.

An interesting example of the multi-stage wave-like transformation with the transition sequence $A \rightarrow N \rightarrow A \rightarrow N \rightarrow A \rightarrow N$ (where A and N mean amorphous and nanocrystalline state, respectively) was observed in the $\text{Ti}_{50}\text{Ni}_{25}\text{Cu}_{25}$ metallic glass after HPT [46]. Fig. 6 shows the crystalline phase volume fraction (V) change as a function of the turns including a part of turn, namely $\frac{1}{4}$ and $\frac{1}{2}$ (adapted from [46]).

It follows from the Fig. 6 data that nanocrystallization of the amorphous phase begins

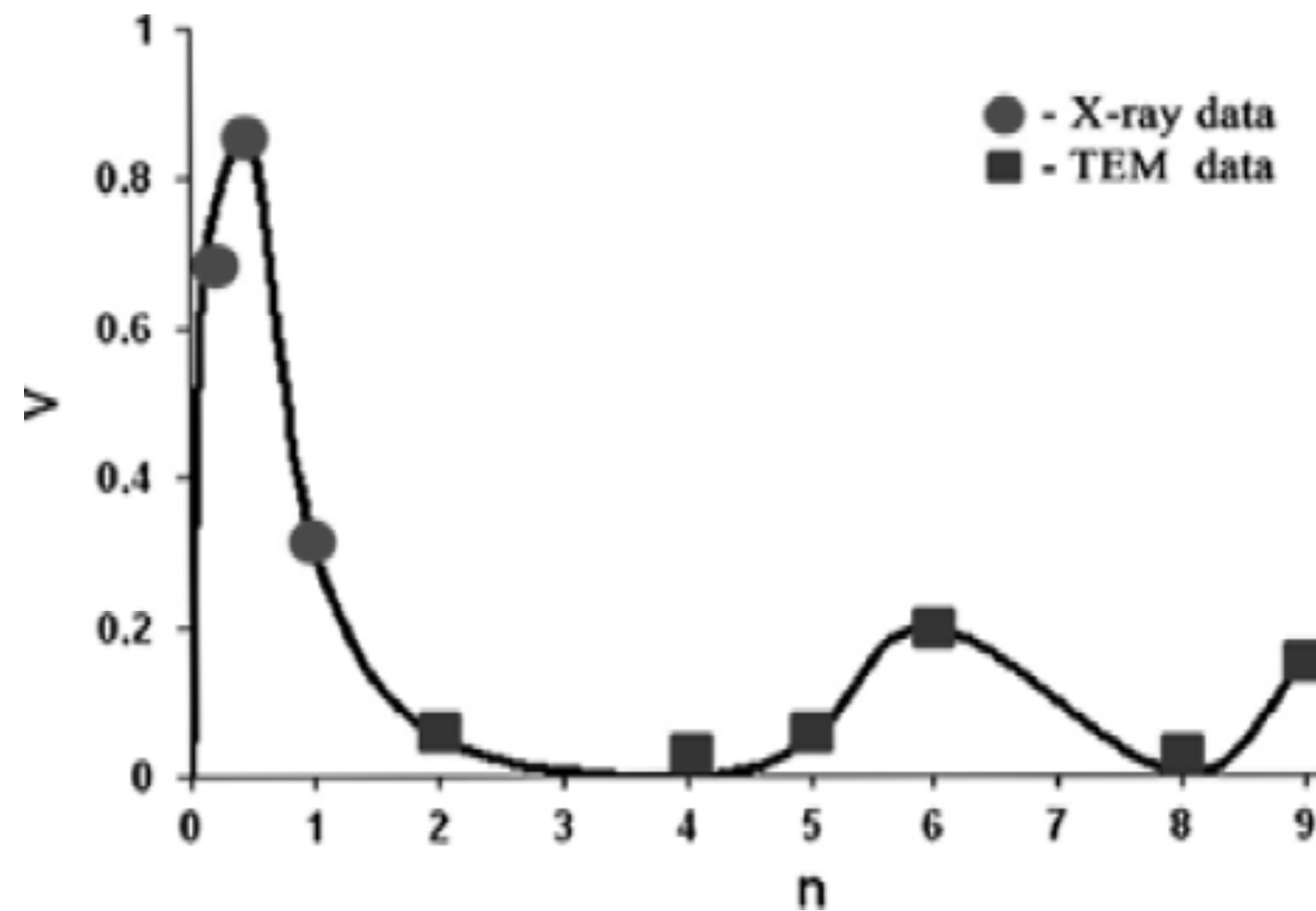


Fig. 6. The effect of the turns (n) during HPT ($P = 4$ GPa, $T = 300$ K) on the crystalline phase volume fraction for $\text{Ti}_{50}\text{Ni}_{25}\text{Cu}_{25}$ alloy, adapted from [46].

at very low deformation degree, after which a reverse process starts with wave-form repeats. The authors [46] suggested that such a cyclic character of the $A \leftrightarrow N$ transformation is connected with the dissipation peculiarities of the mechanical energy introduced (in other words, “pumped in”) into the samples during HPT. Various processes of the phase transformations, defects reorganization, dynamic recrystallization, and thermal effects can serve as channels for this energy dissipation mechanism. In the very particulate case, the process depends on numerous factors, such as temperature, pressure, amorphization thermal barrier, etc., and therefore so far the $A \leftrightarrow N$ cyclic transformations remain out of correct predictions.

In several studies, where nanosized TiO_2 powders ($L = 8$ – 20 nm) were subjected to high-pressure actions during impact compression tests ($P = 10$ – 45 GPa, $T = 500$ – 2500 K) with a load duration of several microseconds, it was found that the initial material tetragonal phase (anatase) transforms into either the orthorhombic phase (columbite) or the microcrystalline rutile [47]. For comparison with the TiO_2 behavior under high static pressures, it is appropriate to show the results obtained by synchrotron XRD and Raman spectroscopy (Fig. 7, adapted from [48]).

As can be seen in Fig. 7a, nanocrystals with grain size below of 10 nm undergo pressure-induced amorphization and remain amorphous ($a\text{-TiO}_2$) upon further compression and decompression. In the 12–50 nm range the compression-induced transformation into the monoclinic baddeleyite structure ($m\text{-TiO}_2$) is observed, which transforms into the orthorhombic phase ($o\text{-TiO}_2$) upon decompression. Coarser crystallites with a grain size of above 50 nm transform directly to thermodynamically stable

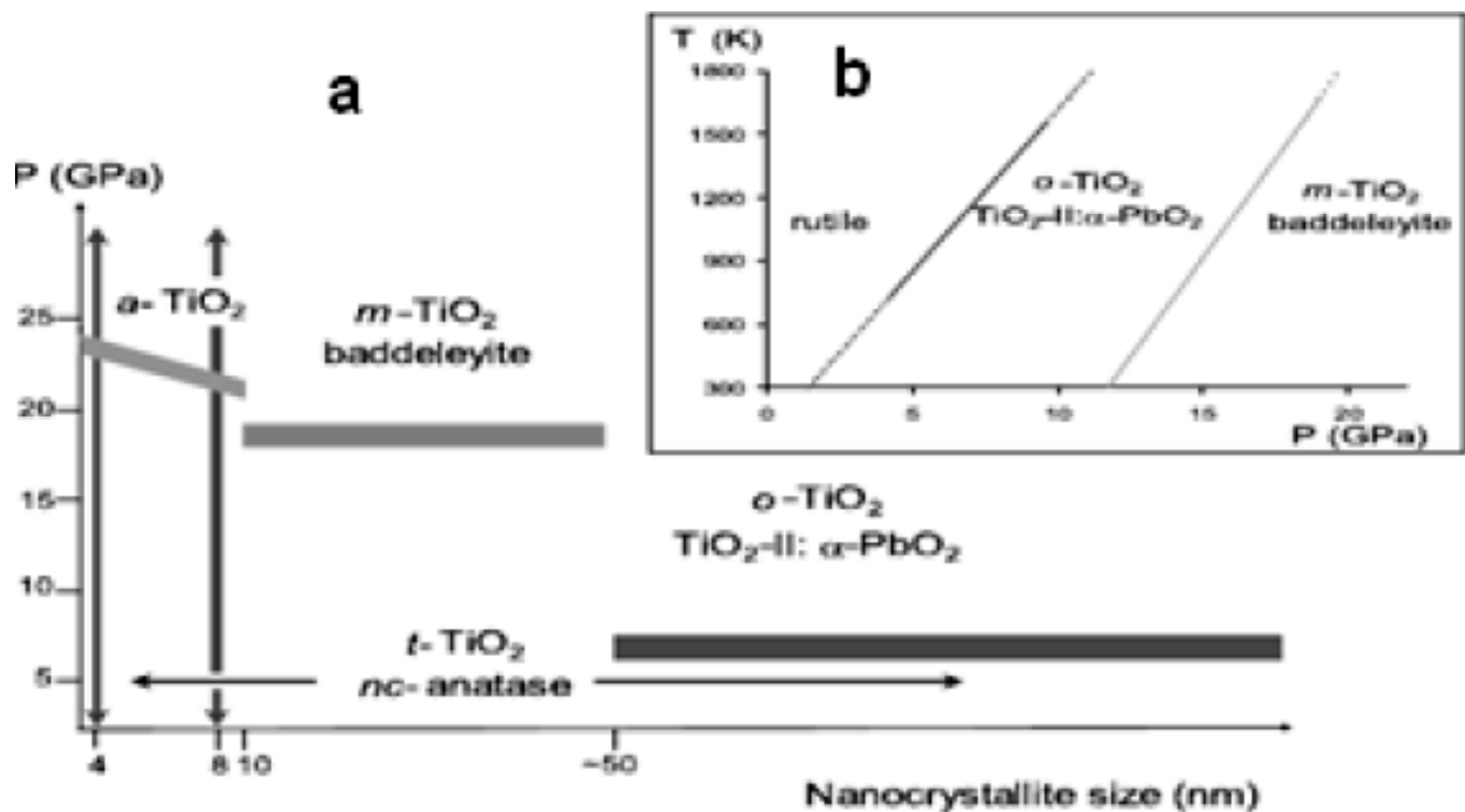


Fig. 7. Size-dependent pressure stability of nano TiO₂ (a) and known P – T relations for bulk TiO₂ samples (b), adapted from [48].

α -TiO₂ phase (TiO₂-II with α -PbO₂ structure). Two compression-decompression paths of the two samples of study [48] indicated. The bulk TiO₂ samples demonstrate their own pressure-induced features (Fig. 7b).

2.3. Other examples of mechanical actions and combined effects

Singh and Kao [49] have generalized many examples of the NMs behavior, such as Ni, Fe–Cu, CdSe, Al₂O₃, CeO₂, CuO, AlN, etc., under high static pressures. It was demonstrated that the volume expansion behavior as a function of pressure up to 50–150 GPa can be described by equations of state using data on the bulk modulus change, and that there is a satisfactory agreement between the theory and experiment results especially in the low pressure range.

The studies of grain growth under deformations (dynamic recrystallization) are now very popular, but most publications are devoted to materials with a CG initial crystal structure, and therefore, we shall only mention some non-trivial investigations. For example, authors [50] considered the evolution of the high-angle grain boundaries formation during HPT at room temperature and the accompanied dynamic recrystallization in some Fe–Ni alloys. In connection with these results, an important observation [51] must be mentioned: a dynamic recrystallization markedly proceeds at room temperature (the grain size growth from 300 nm to 100 μ m) in the crack regions during rotating–bending fatigue testing pro-

cesses in UFG copper. These data confirm the before presented results concerning the grain size influence on the S – N curves characteristics (Figs. 1a and 2a) [28,33]. T. Rupert with coworkers [52,53] have observed interesting results on stress-driven grain growth in nanocrystalline aluminum thin films and grain growth under sliding wear of nanocrystalline Ni–W. Unusual twinning-dominated deformation in nanoscale body-centered cubic W has been revealed using *in situ* high-resolution TEM and atomistic simulations [54].

The NMs behavior under indentation has been investigated in several studies (e.g., [38,55–58]). The examination of grain growth in nanocrystalline Cu under microhardness indenter has revealed that grain coarsening was even faster at cryogenic temperatures than at room temperature and sample purity was seen to play an important role in determining the rate of grain growth [55]. The authors [56] have showed using atomistic simulations that stress-driven grain growth can be obtained in the athermal limit during nanocrystalline aluminum indentation. They found that the grain growth results from rotation of nanograins and propagation of shear bands.

Two other important peculiarities of the NMs behavior under indentation must be marked also: a plastic deformation of some brittle materials [38,57] and their different character under indentation [38,58]. The TiN film fracture surfaces near indentation imprints are shown in Fig. 8. They have a clear-cut columnar structure, whereas the break as a whole has a character of brittle destruction (Fig. 8a), but in some places there are pronounced bends of

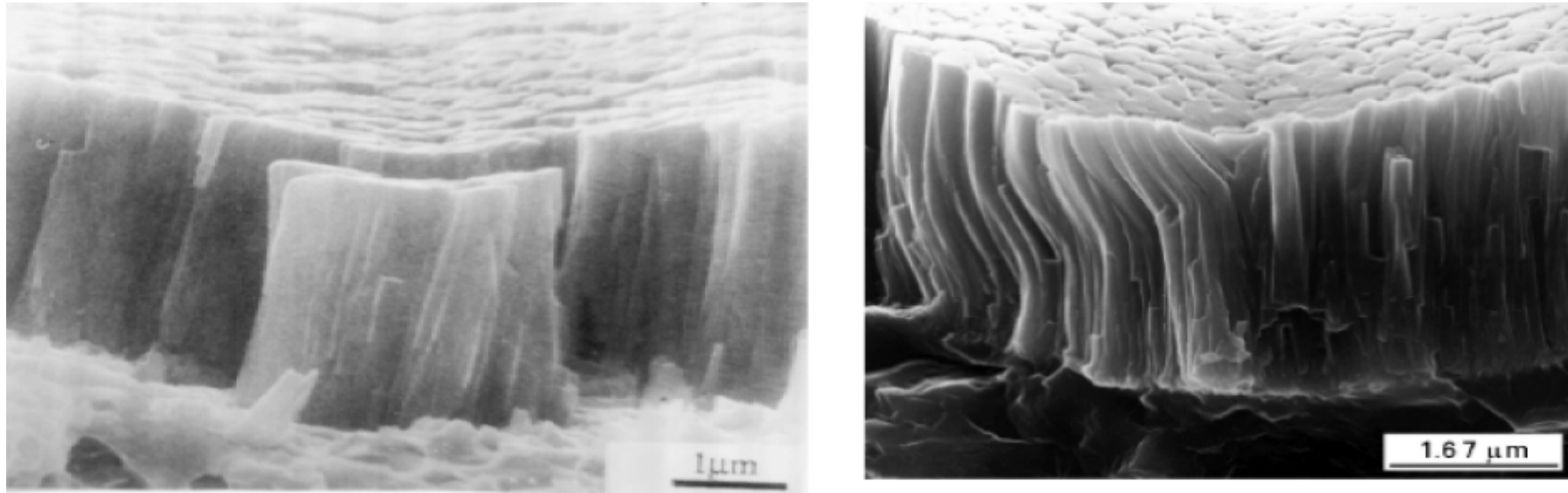


Fig. 8. High-resolution scanning electron microscopy images of the TiN film fracture surfaces in the case of brittle deformation (a) and residual plastic (b) deformation, adapted from [57].

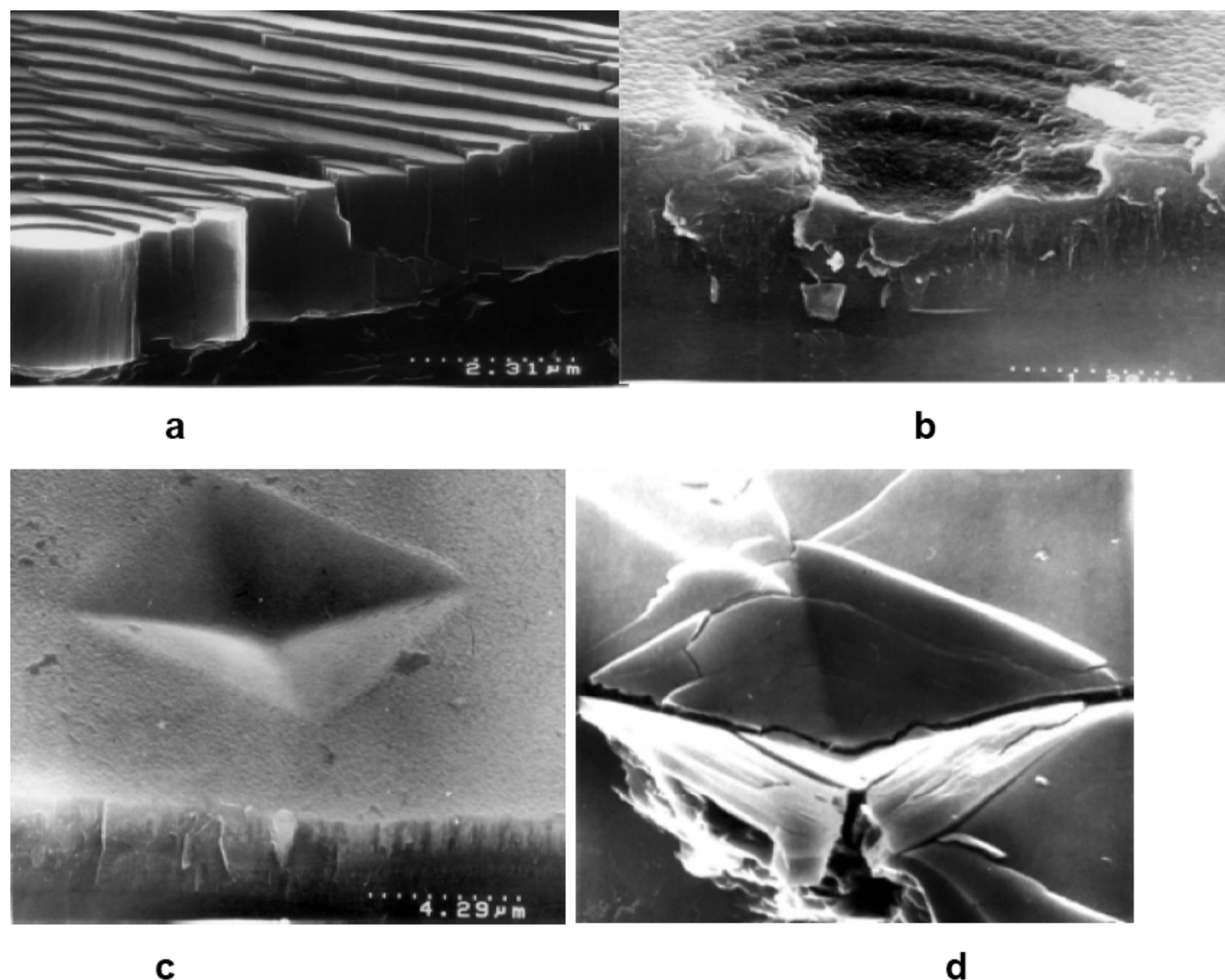


Fig. 9. Indentation imprint surfaces in TiB_2 (a and b) and TiN (c and d), adapted from [58].

the columns, arising naturally under the volume non-uniform compression (Fig. 8b).

The study of imprint surfaces formed after the nanostructured films indentation has demonstrated two deformation types: a non-uniform process with formation of shift bands and steps (TiB_2 ; Figs. 9a and 9b) and a uniform deformation (TiN; Figs. 9c and 9d). The appearance of plasticity in brittle materials and difference in their deformation nature can be connected with special peculiarities of columnar structure of TiN films (Fig. 8) and their sliding over the interfaces [38,57,58], whereas TiB_2 films are characterized by the absence of a columnar structure, and therefore their deformation has a more localized and non-homogenous character.

It seems to be very important to point the stable interface role under extreme plastic deformation. The use of ARB technology proved to be very efficient

for creation of a regular array of atomic-scale facets (i.e., the zig-zag morphology) in nanolayered Cu–Nb materials [59]. The two types of ordered interfaces after very high strains, which decrease the initial thickness by 5–6 orders of magnitude (from 2 mm to 20 nm!) are shown in Fig. 10 (adapted from [59]). The experiments also demonstrated that the interfaces in these Cu–Nb nanolaminates are stable with respect to continued extreme straining (effective strains > 12) as well as to high-temperature and irradiation effects.

A very illustrative example of the application of multifunctional nanocomposite wire Cu–Nb in pulsed high magnetic fields (> 60 T) is described in Refs. [12,60]. The demands for such wire properties are very high and include the following parameters: the strength not below 1 GPa (to resist a great Lorentz force arising in magnetic fields), electrical conduc-

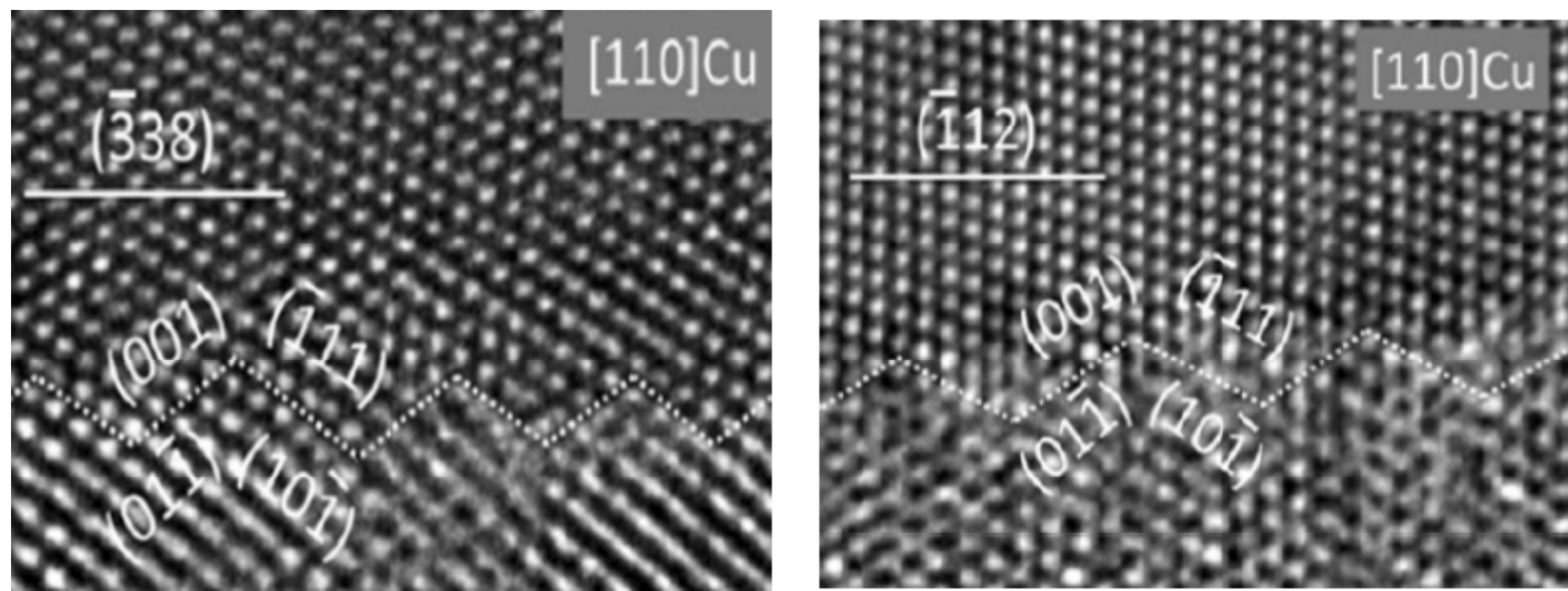


Fig. 10. High-resolution TEM images of preferred Cu–Nb interfaces: (a) $\{338\}\langle 443\rangle$ Cu $\parallel\{112\}\langle 110\rangle$ Nb and (b) $\{112\}\langle 111\rangle$ Cu $\parallel\{112\}\langle 110\rangle$ Nb, adapted from [59].

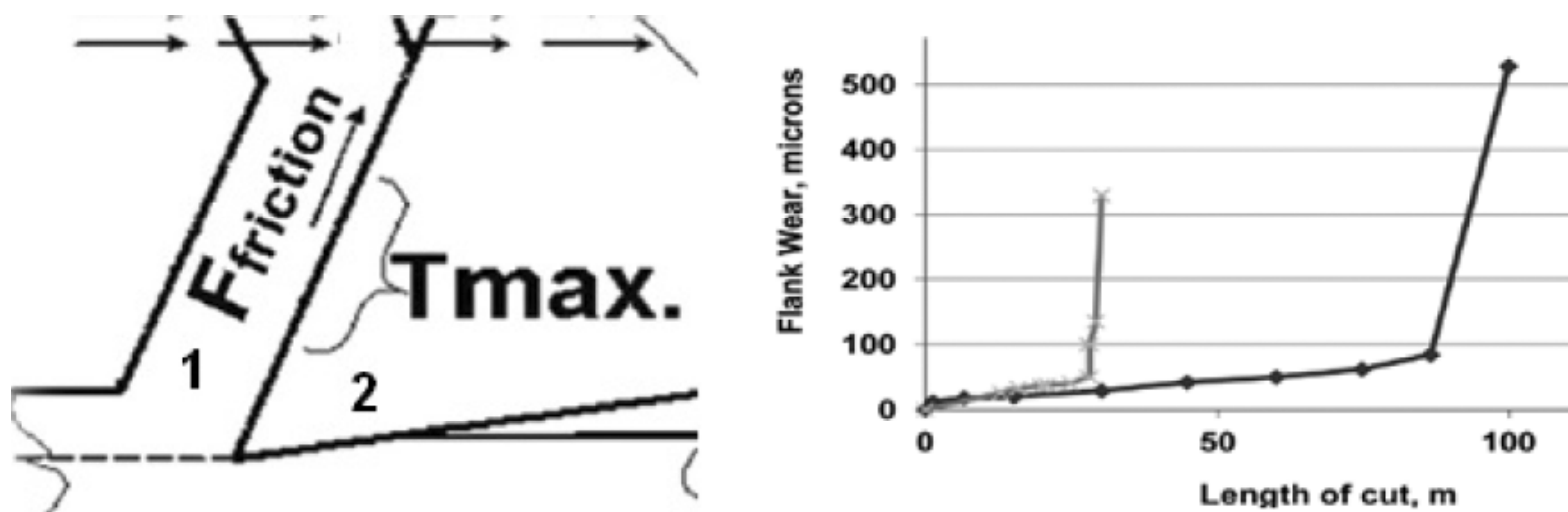


Fig. 11. The scheme of a chip (1) /tool (2) interface during cutting (a) and tool life of one (x)- and multi-layer (■) TiAlCrSiYN-based coatings vs. cutting speed of 600 m/min (b). The total thickness of these coatings was close (about 2 μm); the grain size in one- and multi-layer coatings was below 40 nm and 20–40 nm, respectively.

tivity not below 0.6 the value for pure copper (for the ohmic losses minimization), operational temperature in the 77–673 K range, the fatigue durability over 5000 cycles, and the radiation stability up to He ions flow densities above 10^{15} ions/cm². The structure that meets these tough demands was created by a complex SPD treatment including repeated hot-extrusion, cold drawing, and bundling cycles. Finally, the Cu nanocomposite wire had a diameter of ~2.5 mm with a content of about 20 vol.%Nb fibers with a diameter of ~140 nm. A complex hierarchical and multi-scale character of the described Cu–Nb wire allows this material to be successfully used under the listed extreme actions.

A combination of extreme loads was also studied by Fox-Rabinovich and coworkers [61] using the high-speed cutting treatment of examples. As shown in Fig. 11a (adapted from [61]), herein at the chip/cutting tool interface, the temperature can exceed 1000 °C and the pressure achieves about 1.5 GPa.

The multi-layer coating advantage is obvious from Fig. 11b. It can be connected with a more active formation of a barrier tribo-film, which retards the heat flows propagation and preserves the tool

strength, when the multi-layer TiAlCrSiYN/TiAlCrN coating is used. The prospects of multi-layer nitride coatings, composed of alternating polycrystal CrAlN and nanocomposite CrAlSiN layers for the achievement of high strength and toughness were also marked in review [62].

3. SOME THEORETICAL APPROACHES AND MODELLING

Ovid'ko and his coworkers continue theoretical study of the NMs deformation (e.g., [63–66]). For example, various situation of stable and unstable intergrain boundaries migration under the action of stresses have been analyzed [63], as well as the evolution of nanocracks under deformations has been studied on objects with twins of both bulk and film nanostructures [64].

Fig. 12 (adapted from [64]) illustrates various situations for the nanocrack and the lamella twin ABCD (with thickness h , length d and partial dislocations at boundaries displaced at distance p from each other): 1) generation of a nanocrack in a grain; 2) generation of an intergranular nanocrack; 3) ABCD

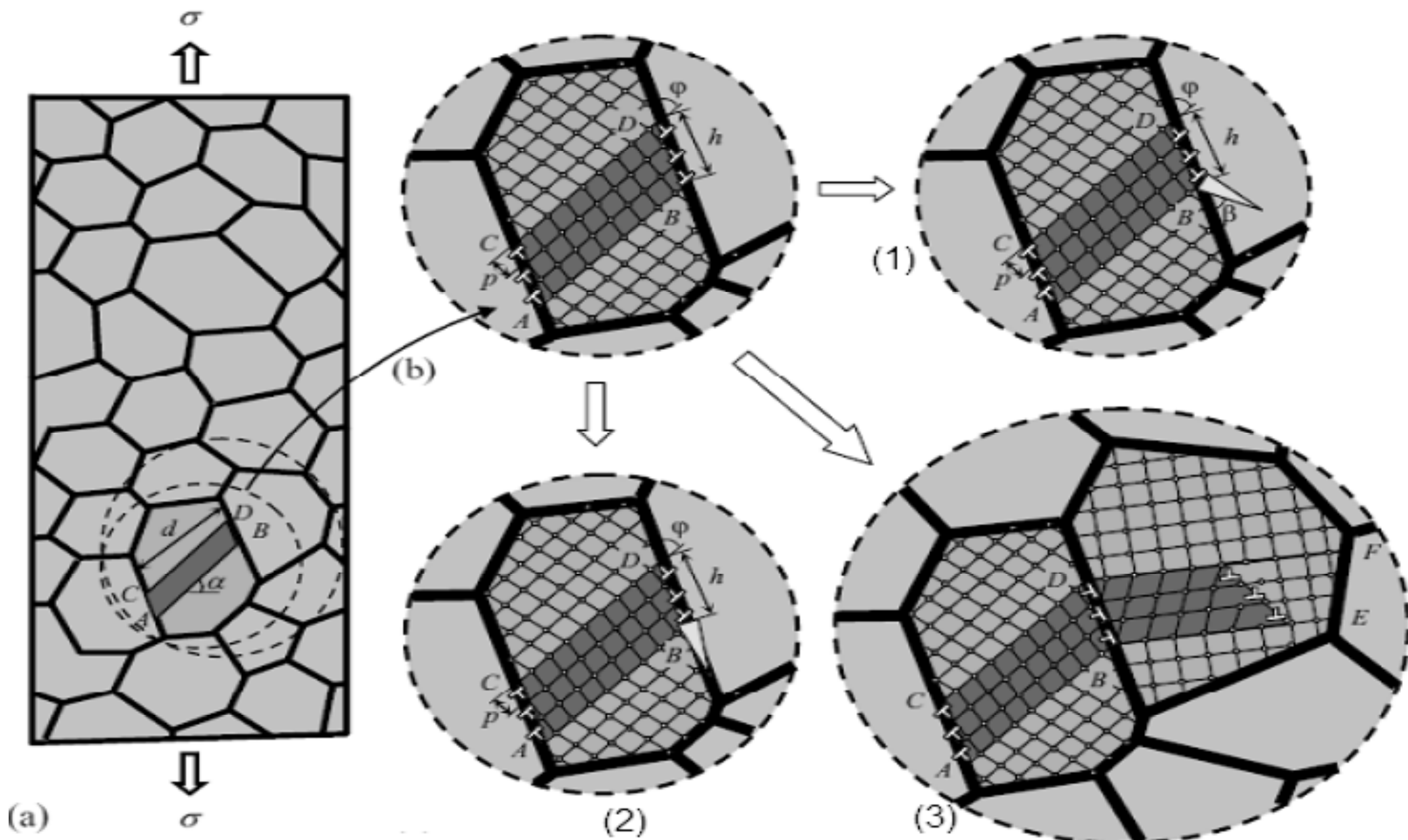


Fig. 12. Schematic views of the twin/nanocrack behavior in deformed NMs: (a) and (b) are general view and magnified inset, correspondingly; (1), (2) and (3) are different versions of behavior (see definitions in text), adapted from [64].

twin transfer into a neighbor grain. The theoretical analysis applied to cubic structures has demonstrated that nanocracks in bulk NMs arise at the twin boundaries (with width of several nm) and intensely grow with increasing twin width h , stress σ , and angle φ . The equilibrium nanocrack length in films markedly decreases, when the spacing between lamella twins, or their distance from the film surface, is below several h values.

In Ref. [65], Mg segregation was studied especially for the processes near low-angle grain boundaries and high-angle those arising under the deformation of UFG Al–Mg alloys. It was found that the boundaries segregation enrichment (earlier fixed in many experimental studies) is provoked by the stress fields of extrinsic dislocations existing near the grain boundaries.

The results of modeling the NMs behavior under mechanical actions are presented in many publications (e.g., [67–69]) and related to various situations. For example, the modeling of fatigue crack growth resistance in NMs by molecular dynamic (MD) and material mechanics methods has revealed that the crack growth processes can be retarded, whenever it is possible to decrease the twin width and the distance between them to the values below 20 nm [67]. A large-scale MD simulation was carried out to evaluate the impact load action (with ve-

locity of 600 m/s) on the nano- and single-crystalline copper samples [68], for which the spall strength and the pore formation parameters were calculated depending on the nanotwin width. The authors concluded that the nanotwin width reduction assists the growth of material mechanical properties only for the action on nanotwinned single-crystalline objects. The same authors, using the large-scale MD simulation, have studied the influence of the hydrostatic pressure on the properties of nanocrystal copper with a grain size of 3–15 nm [69]. The calculations showed that a nanocrystal with 3 nm grain size can become amorphous under a hydrostatic pressure of 80 GPa.

4. CONCLUSIONS

Our overview covers only the main points of the problem, and additional information can be found in Refs. [49,70]. A wide application of mechanical actions in the NMs manufacturing, such as high-energy milling, hot pressing, hot extrusion, techniques of high temperature and high pressure, plasma activated sintering, laser ablation, etc., should be also borne in mind. Nevertheless, it is quite obvious that NMs themselves can perfectly resist a pretty high mechanical load and have significant potential. In this respect, the gradient surface nanostructures, which

have a high level of strength and ductility as well as proved to be stable under other extreme conditions (e.g., during irradiation and in corrosion environments) [71–73], seem to be particularly promising. There are, however, some unresolved issues, such as the NMs behavior in high-cycle fatigue tests, the role of synergistic effects in combined impacts, etc. Also, it is important to pay attention to the development of optimal nanostructures able to withstand the extreme mechanical and other impacts. All this needs further detailed theoretical and experimental studies

ACKNOWLEDGEMENTS

The author is grateful to V.V. and S.V. Klyucharev for effective help in manuscript preparation. The financial support from the Russian Basic Research Foundation and the Russian Academy of Sciences is appreciated.

REFERENCES

- [1] R.J. Hemley, G.W. Crabtree and M.V. Buchanan // *Phys. Today* **62** (2009) 32.
- [2] V.E. Fortov and V.B. Mintsev // *Russ. Chem. Rev.* **82** (2013) 597.
- [3] N. Bourne, *Materials in Mechanical Extremes – Fundamentals and Applications* (New York, Cambridge University Press, 2013).
- [4] *MAX Phases and Ultra-High Temperature Ceramics for Extreme Environments*, ed. by I.M. Low, Y. Sakka and C.F. Hu (Hershey, IGI Global, 2013).
- [5] *Ultra-High Temperature Ceramics. Materials for Extreme Environment Applications*, ed. by W.G. Fahrenholtz, E.J. Wuchina, W.E. Lee and Y. Zhou (New Jersey, The Amer. Cer. Soc., Wiley, 2014).
- [6] M. Rose, A.G. Balogh and H. Hahn // *Nucl. Instr. Meth. Phys. Res. B* **127/128** (1997) 119.
- [7] R.A. Andrievski // *J. Mater. Sci.* **38** (2003) 1367.
- [8] *Nanostructured Coatings*, ed. by A. Cavaleiro and J.T. De Hosson (Heidelberg, Springer, 2006).
- [9] C.C. Koch, I.A. Ovid'ko, S. Seal and S. Veprek, *Structural Nanocrystalline Materials: Fundamentals and Applications* (Cambridge, Cambridge University Press, 2007).
- [10] O. Anderoglu, A. Misra, H. Wang and X. Zhang // *J. Appl. Phys.* **103** (2008) 094322.
- [11] S. Wurster and R. Pippin // *Scr. Mater.* **60** (2009) 1083.
- [12] A. Misra and L. Thilly // *MRS Bull.* **35** (2010) 965.
- [13] R.A. Andrievski // *Rev. Adv. Mater. Sci.* **29** (2011) 54.
- [14] R.A. Andrievski // *Prot. Met. Phys. Chem. Surf.* **49** (2013) 528.
- [15] I.J. Beyerlein, A. Caro, M.J. Demkowicz, N.A. Mara and A. Misra // *Mater. Today* **16** (2013) 443.
- [16] X.C. Liu, H.W. Zhang and K. Lu // *Science* **342** (2013) 337.
- [17] R.A. Andrievski // *J. Mater. Sci.* **49** (2014) 1449.
- [18] B.V. Manesh and R.K. Singh Raman // *Metall. Mater. Trans. A* **45** (2014) 5799.
- [19] R.A. Andrievski // *Physics–Uspekhi* **57** (2014) 947.
- [20] M. Saber, C.C. Koch and R.O. Scattergood // *Mater. Res. Lett.* **3** (2015) 65.
- [21] A.V. Ragulya // *Adv. Appl. Ceram.* **107** (2008) 118.
- [22] Y. Estrin and A. Vinogradov // *Acta Mater.* **61** (2013) 782.
- [23] R.Z. Valiev, A.P. Zhilyaev and T.G. Langdon, *Bulk Nanostructured Materials: Fundamentals and Applications* (Weinheim, Wiley, 2014).
- [24] Y. Estrin and A. Vinogradov // *Int. J. Fatigue* **32** (2010) 898.
- [25] H. A. Padilla II and B.L. Boyce // *Exper. Mech.* **50** (2010) 5.
- [26] I.P. Semenova, G.Kh. Salimgareeva, V.V. Latysh, T. Lowe and R.Z. Valiev // *Mater. Sci. Eng. A* **503** (2009) 92.
- [27] S.V. Dobatkin, V.F. Teren'tiev, W. Skrotzki, O.V. Rybal'chenko, M.N. Pankova, D.V. Prosvirin and E.V. Zolotarev // *Russ. Metallurgy (Metally)* No 11(2012) 954.
- [28] R.H. Li, Z.J. Zhang, P. Zhang and Z.F. Zhang // *Acta Mater.* **61** (2013) 5857.
- [29] T. Hanlon, Y.-N. Kwon and S. Suresh // *Scr. Mater.* **49** (2003) 675.
- [30] P. Zhang, Z.J. Zhang, L.L. Li and Z.F. Zhang // *Scr. Mater.* **66** (2012) 854.
- [31] G.P. Zhang, K.H. Sun, B. Zhang, J. Gong, C. Sun and Z.G. Wang // *Mater. Sci. Eng. A* **483–484** (2008) 387.
- [32] Ch. Ensslen, O. Kraft, R. Mönig, J. Xu, G.-P. Zhang and R. Schneider // *MRS Commun.* **4** (2014) 83.
- [33] L. Yang, N.R. Tau, K. Lu and L. Lu // *Scr. Mater.* **68** (2013) 801.

- [34] H.W. Huang, Z.B. Wang, J. Lu and K. Lu // *Acta Mater.* **87** (2015) 150.
- [35] O.B. Naimark, O.A. Plekhov, V.I. Betekhtin, A.G. Kadomtsev and M.V. Narykova // *Techn. Phys.* **59** (2014) 398.
- [36] P. Lukáš, L. Kunz, L. Navrátilová and G. Bokůvka // *Mater. Sci. Eng. A* **528** (2011) 7036.
- [37] I.-Ch. Choi, B.G. Yoo, O. Kraft, R. Schwaiger, M.-Y. Seok, M. Kawasaki, T.G. Langdon and J.-I. Jang // *Mater. Sci. Eng. A* **618** (2014) 37.
- [38] R.A. Andrievski and A.M. Glezer // *Physics–Uspekhi* **52** (2009) 315.
- [39] A.M. Glezer, E.N. Blinova, V.A. Poznyakov and A.V. Shelyakov // *J. Nanopart. Res.* **5** (2003) 551.
- [40] S.M. Clark, S.G. Prilliman, C.K. Erdonmez and A.P. Alivisatos // *Nanotechnology* **16** (2005) 2813.
- [41] K. Edalati, T. Daio, M. Arita, S. Lee, Z. Horita, A. Togo and I. Tanaka // *Acta Mater.* **68** (2014) 207.
- [42] B.B. Straumal, A.A. Mazilkin, S.G. Protasova, P.B. Straumal, A.A. Myatiev, G. Schütz, E. Goering and B. Baretzky // *Phys. Met. Metallogr.* **113** (2012) 1244.
- [43] B.B. Straumal, S.V. Dobatkin, A.O. Rodin, S.G. Protasova, A.A. Mazytkin, D. Goll and B. Baretzky // *Adv. Eng. Mater.* **13** (2011) 463.
- [44] B.B. Straumal, X. Sauvage, B. Baretzky, A.A. Mazytkin and R.Z. Valiev // *Scr. Mater.* **70** (2014) 59.
- [45] D. Raabe, P.-P. Choi, Y. Li, A. Kostka, X. Sauvage, F. Lecouturier, K. Hono, R. Kirchheim, R. Pippan and D. Embury // *MRS Bull.* **35** (2010) 982.
- [46] R.V. Sundeev, A.M. Glezer and A.V. Shalimova // *Mater. Lett.* **133** (2014) 32.
- [47] A.M. Molodets, A.A. Golyshev and Yu.M. Shul'ga // *Techn. Phys.* **58** (2013) 1029).
- [48] V. Swamy, A. Kuznetsov, L.S. Dubrovinsky, P.F. McMillan, V.B. Prakapenka, G. Shen and B.C. Muddle // *Phys. Rev. Lett.* **95** (2006) 135702.
- [49] M. Singh and M. Kao // *Adv. Nanopart.* **2** (2013) 350.
- [50] A.M. Glezer, V.N. Varjukhin, A.A. Tomchuk and N.A. Maleeva // *Bull. Russ. Acad. Sci. Phys.* **78** (2014) 1022.
- [51] S.Z. Han, M. Goto, J.-H. Ahn, S.H. Lim, S. Kim and J. Lee // *J. All. Comp.* **615** (2014) 5587.
- [52] T.J. Rupert, D.S. Gianola, Y. Gan and K.J. Memker // *Science* **326** (2009) 1686.
- [53] T.J. Rupert and Ch.A. Schuh // *Acta Mater.* **58** (2010) 4137.
- [54] J. Wang, Z. Zeng, Ch.R. Weinberger, Z. Zhang, T. Zhu and S.X. Mao // *Nature Mater.* **14** (2015) 594.
- [55] K. Zhang, J.R. Weertman and J.A. Eastman // *Appl. Phys. Lett.* **87** (2005) 061921.
- [56] F. Sansoz and V. Dupont // *Appl. Phys. Lett.* **89** (2006) 111901.
- [57] R.A. Andrievski // *Bull. Russ. Acad. Sci. Phys.* **73** (2009) 1222.
- [58] R.A. Andrievski, G.V. Kalinnikov and D.V. Shtansky // *Phys. Sol. State* **42** (2000) 760.
- [59] I.J. Beyerlein, J.R. Mayeur, S. Zheng, N.A. Mara, J. Wang and A. Misra // *Proc. NAS* **111** (2014) 4386.
- [60] J.-B. Dubois, L. Thilly, P.-O. Renault and F. Lecouturier // *Adv. Eng. Mater.* **14** (2012) 998.
- [61] G.S. Fox-Rabinovich, J.L. Endrino, M.H. Aguirre, B.D. Beake, S.C. Veldhuis, A.I. Kovalev, I.S. Gershman, K. Yamamoto, Y. Losset, D.L. Wainstein and A. Rashkovskiy // *J. Appl. Phys.* **111** (2012) 064306.
- [62] Y.X. Wang and S. Zhang // *Surf. Coat. Techn.* **258** (2014) 1.
- [63] M.Yu. Gutkin, K.N. Mikaelyan and I.A. Ovid'ko // *Phys. Sol. State* **50** (2008) 1266.
- [64] I.A. Ovid'ko and A.G. Sheinerman // *J. Phys. D Appl. Phys.* **47** (2012) 015307.
- [65] I.A. Ovid'ko, A.G. Sheinerman and R.Z. Valiev // *J. Mater. Sci.* **49** (2014) 6682.
- [66] S.V. Bobylev and I.A. Ovid'ko // *Rev. Adv. Mater. Sci.* **41** (2015) 20.
- [67] P.B. Chowdhury, H. Sehitoglu, R.G. Raiteick and H.J. Maier // *Acta Mater.* **61** (2013) 2531.
- [68] F. Yuan and X. Wu // *Phys. Rev. B* **86** (2012) 134198.
- [69] F. Yuan and X. Wu // *Comp. Mater. Sci.* **85** (2014) 8.
- [70] A. San-Miguel // *Chem. Soc. Rev.* **35** (2006) 876.
- [71] K. Lu // *Science* **345** (2014) 1455.
- [72] R.A. Andrievski // *Diffus. Found.* **5** (2015) 147.
- [73] R.A. Andrievski and A.V. Khatchoyan, *Nanomaterials in Extreme Environments – Fundamentals and Applications* (Heidelberg, Springer, 2016).